CrossMark

New insights from inviscid modelling of starting flow separation with roll-up

A. C. DeVoria[1] and K. Mohseni[1,2],†

[1]Department of Mechanical & Aerospace Engineering, University of Florida, Gainesville, FL 32611, USA

[2]Department of Electrical & Computer Engineering, University of Florida, Gainesville, FL 32611, USA

This paper investigates the use of inviscid flow theory accompanied by surfaces of discontinuity as a means of representing viscous effects. The problem studied is that of starting flow separation past a sharp wedge. We use the vortex-entrainment sheet model of DeVoria & Mohseni (*J. Fluid Mech.*, vol. 866, 2019, pp. 660–688) to augment the set of self-similar solutions with zero entrainment as calculated by Pullin (*J. Fluid Mech.*, vol. 88, 1978, pp. 401–430). Even under the constraints of similarity, the inclusion of entrainment allows for several new degrees of freedom, which correspond to different classes of boundary conditions, and thus solutions, that are excluded by classical potential models. Some computed examples are presented and compared to a previous experimental study. The results offer encouraging evidence that viscous or finite Reynolds number effects can, in an integrated sense, be captured by an inviscid model with singularity distributions. A normal boundary condition that contains the information pertaining to the entrainment must be supplied and represents the trade-off in surrendering the Navier–Stokes equations for the lower-order inviscid model.

Key words: vortex dynamics

---

1. Introduction

Inviscid models are useful tools for prediction as well as cheaper alternatives to fully resolved simulations. Recently, the authors developed an inviscid model for viscous shear and boundary layers termed a vortex-entrainment sheet (DeVoria & Mohseni 2019). This irregular surface is the superposition of a conventional vortex sheet having a discontinuity in the tangential velocity (i.e. harmonic potential) with an entrainment sheet having a discontinuity in the normal velocity (i.e. streamfunction). The former accounts for the vorticity in the real layer, while the latter accounts for its mass/momentum. It was proposed that the inclusion of entrainment in a model of this type could capture integral viscous-fluid phenomena, e.g. resistive drag, that are notably absent from conventional potential flow models.

In this paper, we further advocate and demonstrate the ability to represent viscous effects within our inviscid vortex-entrainment sheet model. For this express purpose we augment the set of self-similar solutions computed by Pullin (1978) for the roll-up of conventional vortex sheets shedding from a sharp wedge. Pullin's seminal work has been

† Email address for correspondence: mohseni@ufl.edu

highly influential in subsequent investigations that have marked continued advancements in the study of unsteady vortex dynamics. His paper will be liberally cited here and so it will henceforth be referred to simply as 'Pullin'.

The forfeiture of the Navier–Stokes equations in favour of the inviscid model with an infinitely thin sheet bypasses the computational expense of resolving the detailed distributions of the velocity and vorticity across the viscous layer. However, we must inevitably incur this cost elsewhere, in part at least, if the viscous effects are to be captured in some integrated or even global sense. In short, we must supplement the inviscid model with boundary conditions that ideally contain the same level of information as those accompanying the Navier–Stokes equations. For example, the higher-order viscous equation allows one to impose the full velocity vector on the boundaries (with some mass conservation constraint for incompressible flows), which is not generally possible for the lower-order inviscid equation. One way of conveying more of this information to the inviscid model is to specify the normal velocity at the boundaries. In effect, this condition provides the zero-thickness sheet with the entrainment associated with the viscous layer that it replaces. The conventional vortex sheet is technically a special case of this, for which the entrainment is specified to be zero on all boundaries.

The vortex-entrainment sheet has a complex/vector strength and we introduce $\nu = q/\gamma$ as the 'strength ratio' of the entrainment sheet strength q to the vortex sheet strength γ. The entrainment is signed relative to the flow inside the sheet. Namely, $q > 0$ means a net amount of mass/fluid enters the sheet, whereas $q < 0$ means fluid emanates from the sheet. Pullin's solutions correspond to $\nu = 0$ on all boundaries. In two dimensions, the velocity induced by the sheet at an arbitrary point z in an otherwise unbounded domain can be expressed by the following generalized Birkhoff–Rott equation, i.e. Cauchy-type integral (DeVoria & Mohseni 2019):

$$\frac{1}{2\pi i} \int_{a(t)}^{b(t)} \frac{\gamma(s, t) - iq(s, t)}{z - z_s(s, t)} \, \mathrm{d}s. \tag{1.1}$$

The integration is over the sheet whose position at time t is $z_s(s, t)$ with $s \in [a, b]$ as the arclength coordinate. In general, the dynamics of the sheet is governed by 'surface equations' resembling the Euler equations with a sheet density ρ_s (mass per unit area) and with additional source terms representing the entrainment/flux of mass and momentum. Once the normal velocity boundary condition is specified, the outer potential flow problem can be solved and the mass flow into the vortex-entrainment sheets calculated. For the case of a solid body geometry, the sheet fixed to its surface represents the boundary layers and their entrainment. Here, the additional momentum terms include the stress jump across the sheet. As such, the stress on the surface side can be evaluated and integrated to give an estimate of the force on the body, which includes a viscous effect owing to the entrainment. For more details, the interested reader is referred to DeVoria & Mohseni (2019).

Since our aim here is to obtain self-similar solutions to the outer problem, we bypass the surface equations by searching for solutions that are governed by (1.1) when $z \to z_s$. Dynamically, this means the pressure jump across the sheet (supported by $\rho_s \neq 0$) is such that the sheet moves with the average of the discontinuous velocities on each side of the sheet, namely the principal value. Of course, when the sheet contains no mass and has zero entrainment, the equation of motion reduces to the conventional kinematic Birkhoff–Rott equation for a massless vortex sheet.

The Lagrangian formulation used by Rott (1956) and Birkhoff (1962) substitutes the arclength s (or some scalar parameter) for the amount of circulation $\Gamma(s, t)$, as measured from a reference point on the sheet, via the relationship $\gamma = \partial \Gamma / \partial s$. This approach has

been used by many authors in the study of vortex sheet dynamics (e.g. Moore 1979; Krasny 1987; Jones 2003) as it has several utilities stemming from the transformal invariance of the circulation. Analytically, this requires that Γ is a monotonic function of the Lagrangian parameter with an injective inverse. Physically, this represents the continual generation of vorticity of one sign, which here leads to a power-law growth (a functionality typical to similarity solutions) of total circulation in the sheet.

For the vortex-entrainment sheet we now employ the strength ratio $\nu(s, t)$ in order to use the Lagrangian formulation. As such, (1.1) becomes

$$\frac{1}{2\pi i} \int_0^{\Gamma_s(t)} \frac{1 - i\nu(\Gamma', t)}{z - z_s(\Gamma', t)} \, \mathrm{d}\Gamma', \tag{1.2}$$

with $\Gamma_s(t)$ as the total amount of circulation in the sheet at time t. In § 2 we apply the above framework to a generalized problem for the case of starting flow over an infinite wedge with separation, which is then simplified to a self-similar problem in § 3. Several sets of numerical solutions are presented and discussed in §§ 4 and 5, with comparison to experiment in § 4.3. The novel objective of the paper is to draw plausible physical connections between entrainment in the inviscid sheet model and viscous effects.

2. General problem formulation

The attached flow around the wedge is given by a known complex potential $W_o(z, t)$. This flow is singular at the wedge apex and is regularized by allowing separation at the sharp edge to form the free sheet. Formally, the potential $W_o(z, t)$ is obtained as a transformation from a virtual domain with complex variable ζ, where $W_o(\zeta, t) = \sum_{k=-\infty}^{\infty} A_k(t)\zeta^k$ is a Laurent series expansion about $\zeta = 0$ and, in general, the coefficients are complex: $A_k(t) \in \mathbb{C}$ (e.g. see Batchelor 1967, pp. 128, 410). The series that is convergent near $|\zeta| = 0$ has $A_k = 0$ for $k < 0$. For the wedge of internal angle $\beta\pi (0 < \beta < 1)$ and bisector along the real axis in the physical domain, the transformation $\zeta = z^n$ with $n = 1/(2 - \beta)$ maps the wedge faces to the imaginary axis $\zeta = iy^*$ (see figure 1). We then have

$$W_o(z, t) = A_0(t) + A_1(t)z^n + A_2(t)z^{2n} + \cdots + A_k(t)z^{kn} + \cdots . \tag{2.1}$$

Since $\frac{1}{2} < n < 1$, then in the limit $z \to 0$ the dominating, singular term in the velocity expression, $\mathrm{d}W_o/\mathrm{d}z$, of this attached flow is the $k = 1$ term. However, we note that retention of other terms in the series (including $k < 0$ ones) offers a more generalized description of the flow and allows more topologically rich features to occur. Such possibilities are beyond the scope of the current paper, however, and are reserved for future work. Moving on, we may also take $A_0 = 0$ or, equivalently, define $W_o' = W_o - A_0$ without affecting the velocity. Hence, for $|z| \ll 1$ the complex potential is taken as $W_o = A_1(t)z^n$ and represents the mapping of an instantaneously uniform flow in the virtual domain to the physical domain. Pullin considered the vertical component of this uniform flow so that $A_1(t)$ was purely imaginary. Here, we consider an arbitrarily oriented stream and write

$$A_1(t) = U_n(t) - iU_t(t) \rightarrow \frac{\mathrm{d}W_o}{\mathrm{d}z} = nz^{n-1}\{U_n - iU_t\}. \tag{2.2}$$

Going forward, U_t and U_n will be referred to as 'virtual velocities' having dimensions $[L]^{2-n} \cdot [T]^{-1}$, which when multiplied by the mapping derivative $\mathrm{d}\zeta/\mathrm{d}z = nz^{n-1}$ yield a physical velocity.
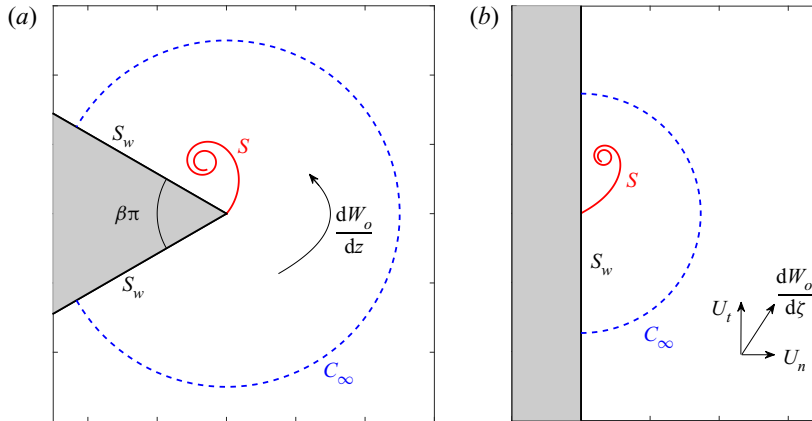
FIGURE 1. Problem geometry and definitions used in this paper. The wedge angle is $\beta\pi$. The analytic fluid domain is given by the simply connected region bounded by the freely shed sheet S, the wedge surface sheet S_w and the arc C_∞ at infinity. Mass entrainment may occur on the vortex-entrainment sheets S and S_w, whereas C_∞ is an ordinary curve across which fluid simply passes. (*a*) Physical *z*-plane with dW_o/dz as the attached driving flow. (*b*) Virtual ζ-plane defined by the mapping $\zeta = z^n$ with $dW_o/d\zeta = U_n - iU_t$ as the uniform virtual velocity whose components are tangential and normal to the mapped wedge boundary.

By superposition, the external flow is combined with the contribution from the free sheet, S, and the sheet representing the wedge surface, S_w, to give the total velocity dW/dz. To have a well-posed problem with a unique solution, we must specify the normal velocity u_n on all boundaries, which includes a contour C_∞ at infinity that intersects the wedge surfaces there (recall figure 1). Stated differently, we must give the entrainment into or flux across each of these boundaries. Note that C_∞ is an ordinary curve with no dynamical significance and is not the location of a discontinuity.

For the free sheet it suffices to give its strength ratio ν. For the wedge surface the boundary condition is typically assumed to be one of no through flow. However, the S_w sheet represents the boundary layers on the wedge and thus any entrainment associated with those layers is given by a non-zero normal velocity. The Cauchy integral for the velocity field is a boundary integral formulation of the solution to the Laplace equation (with kernel appropriate to the geometry) and so the flow at infinity is automatically ensured to have the correct behaviour.

Our end goal of obtaining self-similar solutions is eased if we can eliminate the specification of as many functions and parameters as possible. Our approach to this problem is the method of images. This reduces the degree of freedom from a doubly infinite set to a singly infinite one by providing a relation for the velocity contribution from the wall sheet in terms of the parameters defining the free sheet. In other words, specifying either u_n on the wall or ν on the free sheet will, in principle, determine the other.

The image system is not unique, however. The parameters defining a given sheet are its position and strength, both of which are complex quantities. To allow for some generality, we define the image system with four degrees of freedom as follows. The position in the virtual domain, z_i^n, is taken to be a scaling and rotation of the standard 'mirror image': $z_i^n = -\overline{A^n z_s^n}$, where $A = M e^{i\Theta}$ is to be given; an overbar denotes the complex conjugate. Next, we write the strength of the image sheet as $-(c_\gamma \gamma - ic_q q)$, where c_γ and c_q are two real

constants also to be given; $c_\gamma = 1$ corresponds to the negative of the vortex sheet strength as is usually used. For convenience we define $\chi = (1 - iv)$ and $\chi_i = -(c_\gamma - ic_q v)$, and so the expression for the velocity field becomes

$$\frac{dW}{dz} = nz^{n-1} \left\{ (U_n - iU_t) + \frac{1}{2\pi i} \int_0^{\Gamma_s} \left[\frac{\chi'}{z^n - z_s'^n} + \frac{\chi_i'}{z^n - z_i'^n} \right] d\Gamma' \right\}, \qquad (2.3)$$

where $\chi' = \chi(\Gamma')$ and so on, and explicit time dependence has been dropped for clarity. If u_t and u_n are the tangential and normal physical velocity components on the wedge faces, where $arg\{z^n\} = n\theta = \pm\pi/2$, then the velocity/boundary condition there becomes

$$u_t - iu_n = \pm nr^{n-1}\{(U_t + u_t^*) + i(U_n + u_n^*)\}, \qquad (2.4)$$

where u_t^* and u_n^* are the corresponding tangential and normal virtual velocities (i.e. having units $[L]^{2-n} \cdot [T]^{-1}$) on the wedge. The removal of the singularity in each physical velocity component at $r = |z| = 0$ requires that

$$0 + i0 = (U_t + iU_n) - \frac{1}{2\pi} \int_0^{\Gamma_s} \left[\frac{\chi}{z_s^n} + \frac{\chi_i}{z_i^n} \right] d\Gamma. \qquad (2.5)$$

This is a complex/vector Kutta condition so that we have an additional condition to impose (the imaginary part) as compared to the baseline case of zero entrainment everywhere that was treated by Pullin. Physically, these conditions determine the total circulation Γ_s and net entrainment rate Q_s in the free sheet.

One usually thinks of specifying the normal velocity u_n on the wedge surface as the boundary condition, which will close the problem. However, this leads to an inverse problem for $v(\Gamma, t)$ that is ill conditioned in the same way as Fredholm integrals of the first kind. Alternatively, if v is known, then the problem becomes well posed and the solution unique. We need only give a 'normalized' distribution of v since the imaginary part of the vector Kutta condition is sufficient to determine $Q_s = \int v \, d\Gamma$, which is a scalar quantity. We note that the conventional vortex sheet is a special case of this approach, whereby one imposes the strength ratio to be identically zero on the sheet.

In summary, since we are prescribing the (normalized) strength ratio v of the free sheet, then for the general case we have a seven-parameter solution family: n for the wedge geometry, U_t and U_n specifying the driving flow, and c_γ, c_q, M and Θ defining the wall normal boundary condition (i.e. the image system). The unknowns to be obtained from the solution are the sheet position z_s, its total circulation Γ_s, and its net entrainment rate Q_s.

2.1. The boundary condition at infinity

The expansion in (2.1) was introduced in the context of a convergent series near the apex, $r \to 0$. However, the domain in our mathematical problem is radially infinite and we may consider the behaviour at infinity through a similar series, although it need not be convergent insofar as $W(z)$ is concerned. This multi-pole expansion combines fundamental solutions of the two-dimensional Laplace equation (known as circular harmonics) and generally contains a logarithmic term. From the $r \to \infty$ limit on (2.3) it can be shown that this logarithmic term corresponds to the contribution W_s from the free sheet

(and its image). Specifically, the total complex potential approaches

$$W = W_o + W_s = z^n(U_n - iU_t) + \frac{1}{2\pi i}[(1 - c_\gamma)\Gamma_s - i(1 - c_q)Q_s] \log z^n. \qquad (2.6)$$

The velocity induced by the sheet at infinity is therefore equivalent to that of a point singularity of strength $n[(1 - c_\gamma)\Gamma_s - i(1 - c_q)Q_s]$ located at the apex. However, this velocity decays faster than the driving flow: z^{-1} vs. $z^{-(1-n)}$. Hence, by (2.4) the normal velocity on the wedge surfaces at infinity must approach $u_n = \mp nr^{n-1}U_n$.

The total circulation around and the total mass flux across all boundaries must be zero; these requirements are sometimes called compatibility conditions. Since W_o is itself a solution to the Laplace equation, then it independently satisfies these constraints. Therefore, we may reduce the compatibility conditions as applied to just the flow induced by the sheet and its image

$$\Gamma_s + \Gamma_w = \Gamma_\infty, \quad Q_s + Q_w = Q_\infty, \qquad (2.7a,b)$$

where Q_∞ is the net flux across C_∞ due to the sheet-induced flow there and likewise for Q_w as the net entrainment associated with the wedge S_w; similar definitions apply to Γ_∞ and Γ_w as the corresponding circulations on these boundaries. Integrating the expression for dW_s/dz along the arc C_∞ we obtain the following additional relations:

$$\Gamma_\infty = \tfrac{1}{2}(1 - c_\gamma)\Gamma_s, \quad Q_\infty = \tfrac{1}{2}(1 - c_q)Q_s. \qquad (2.8a,b)$$

We immediately see how the choices of c_γ and c_q affect the flow at infinity. By substitution into (2.7a,b), there are similar consequences for the wall quantities Γ_w and Q_w.

Before continuing, we will find the following quantity useful in non-dimensionalizing the problem. For any sheet, segment of sheet, or arc we define

$$\Gamma - iQ = \Gamma(1 - i\tilde{v}), \qquad (2.9)$$

so that $\tilde{v} = Q/\Gamma$ is the ratio of the flux to the circulation associated with the curve. For a vortex-entrainment sheet with $\Gamma - iQ = \int(1 - iv)\,d\Gamma$, then $\tilde{v}$ is the average of $v(\Gamma)$ on the curve, e.g. $\tilde{v}_s = Q_s/\Gamma_s$ for the free sheet. For an arc that is not the location of a discontinuity, then $\Gamma - iQ = \int(u_t + iu_n)\,dl$ as usual. In particular, the attached driving flow, dW_o/dz, defines $\tilde{v}_o = Q_o/\Gamma_o = -U_n/U_t$ on the arc C_∞ at infinity.

3. The self-similar problem

Here, we identify the restrictions that are required for a solution to be self-similar. First, the similarity form and variable are defined as

$$z_s(\Gamma, t) = L(t)\omega(\lambda), \quad \lambda = 1 - \frac{\Gamma}{JG(t)}, \qquad (3.1)$$

where $L(t)$ is a time-dependent physical length scale, $\omega(\lambda) = \xi(\lambda) + i\eta(\lambda)$ is the self-similar shape function with similarity variable λ, and $G(t)$ is the temporal growth of Γ with J as a non-dimensional constant corresponding to the total circulation. Note that Γ is defined as the circulation between a point $z_s(\Gamma, t)$ and the rolled-up tip of the sheet where $\lambda = 1$. At the apex $\lambda = 0$ and so $\Gamma_s = JG$.

Writing $U_t(t) = \dot{Y}(t)$ we first find that $C_o = (L^{1-n}\dot{L})/\dot{Y}$ must be a non-dimensional constant; recall that $U_t = \dot{Y}$ has units $[L]^{2-n} \cdot [T]^{-1}$. The next constraint for the solution to be self-similar is

$$Q_P = \frac{\dot{G}/G}{\dot{L}/L} = n + (2-n)\frac{Y\ddot{Y}}{\dot{Y}^2} = \text{const.} \tag{3.2}$$

The symbol Q_P is not to be confused with an entrainment rate; the subscript 'P' indicates 'Pullin' who used Q with no subscript for this term. Hence, the (logarithmic) growth of the circulation must be proportional to that of the sheet size. The further constraint $Y\ddot{Y} \propto \dot{Y}^2$ implies that the work required to move the wedge with 'virtual velocity' $\dot{Y}$ is proportional to its kinetic energy. The power-law form $\dot{Y}(t) = a(t+b)^m$ satisfies this condition irrespective of the values a and b, and gives $Q_P = (n+2m)/(1+m)$. The exponential law $\dot{Y}(t) = ae^{bt}$ is also valid and represents the $m \to \infty$ limit of the algebraic form. We adopt the former choice with $b = 0$ (as did Pullin), and the length scale then becomes

$$L(t) = [C(at^m)t]^{1/(2-n)}, \tag{3.3}$$

with $C = C_o(2-n)/(1+m)$ as another non-dimensional constant. Next, the differential circulation is

$$\frac{-\mathrm{d}\Gamma}{L^n \dot{Y}} = \frac{JG(t)\,\mathrm{d}\lambda}{(L^2/t)/C}, \tag{3.4}$$

which gives $G(t) = (L^2/t)/C = (L\dot{L})/C_o$. Following Pullin, the constant C_o is taken as $C_o = (1-n)$ and so (2.3) finally becomes the following integro-differential equation:

$$(1-n)\left[\bar{\omega} + Q_P(1-\lambda)\frac{\mathrm{d}\bar{\omega}}{\mathrm{d}\lambda}\right] = \frac{\mathrm{d}\Omega}{\mathrm{d}\omega}, \tag{3.5a}$$

$$\frac{\mathrm{d}\Omega}{\mathrm{d}\omega} = n\omega^{n-1}\left\{-i(1-i\tilde{v}_o) + \frac{J}{2\pi i}\int_0^1 \left[\frac{\chi'}{\omega^n - \omega'^n} + \frac{\chi_i'}{\omega^n - \omega_i'^n}\right]\mathrm{d}\lambda'\right\}, \tag{3.5b}$$

where $\omega_i^n = -\overline{A^n\omega^n}$ is the image sheet, $\Omega(\omega)$ is the non-dimensional complex potential and again $\tilde{v}_o = Q_o/\Gamma_o = -U_n/U_t$. The vector Kutta condition in (2.5) takes the following non-dimensional form:

$$0 = (1-i\tilde{v}_o) - \frac{J}{2\pi}\int_0^1 \left[\frac{\chi}{\omega^n} + \frac{\chi_i}{\omega_i^n}\right]\mathrm{d}\lambda. \tag{3.6}$$

The quantity $\tilde{v}_o$ may, in general, be a function of time. This is permissible because the Laplace equation is elliptic and all other time dependency in (3.5) has been removed. Hence, the spatial problem can be solved with the instantaneous value. In this way, a separate implicit time dependence can exist in the solution as $z_s(t) = L(t)\omega(\lambda; \tilde{v}_o(t))$, which allows the actual sheet shape to evolve in a more complex way. The same is also true for the other input parameters in the problem (see figure 5 and corresponding discussion in § 4.3).

For the non-dimensional, self-similar problem the driving flow is now specified by m and $\tilde{v}_o$, while the parameters describing the wedge geometry and the image system remain the same. The normal boundary condition on the wedge at infinity is $u_n = \pm nr^{n-1}\tilde{v}_o$. The unknowns to be found are the sheet position ω, its total circulation J and its average strength ratio $\tilde{v}_s = Q_s/\Gamma_s$.

3.1. *Approximation of the core region*

Due to the tightly wound turns within the rolled-up spiral, it is not very sensible to fully resolve (3.5) in this region. Instead, it is common to replace the core region with an isolated point singularity that connects to the severed sheet via a branch cut. The motion of this singular point is determined by imposing a 'zero-net-force' condition on the branch cut system, representing the conservation of linear momentum. We adopt the usual model that balances a pressure jump force acting on the cut with a Joukowski force acting on the point (Brown & Michael 1954; Rott 1956). Here, the Joukowski force will have a conjugate contribution from the entrainment constituent.

First, by (2.9) the complex strength of the singular core point is $\Gamma_c(1 - i\tilde{v}_c)$, where $\tilde{v}_c$ is the average of the strength ratio in the core region. In terms of the similarity variables the non-dimensional strength is $J(1 - \lambda_c)(1 - i\tilde{v}_c)$ with λ_c as the value of λ where the cut has been made. Likewise, the zero-force condition serving as the governing equation for the point is

$$\left.\frac{d\Omega}{d\omega}\right|_{\omega_c} = (1 - n)\left[\bar{\omega}_c + Q_P\left(\frac{\bar{\omega}_c - \bar{\omega}_s}{1 - i\tilde{v}_c}\right)\right], \tag{3.7}$$

where ω_c and ω_s are the locations of the singular core point and the end of the severed sheet, respectively. The above was used by Pullin with $\tilde{v}_c = 0$, although he did not explicitly give this equation.

3.2. *Asymptotic solution near the apex*

By analytically enforcing the Kutta condition Pullin obtained the asymptotic solution for $\omega(\lambda)$ very near the wedge apex ($\lambda \to 0$). He showed that the vortex sheet must shed tangential to the windward wedge face, while the flow on the leeward face is consequently stagnated at the apex and thus has no contribution to the free sheet. The details of the analogous process for the vortex-entrainment sheet are provided in appendix A and here we simply state the results. Also, we take $U_t > 0$ going forward.

The vortex-entrainment sheet has a continuously variable shedding angle θ_a at the apex. Defining $c_a = c_q v_a / c_\gamma$ where $v_a = v(0)$ is the strength ratio at the apex, then θ_a is given by

$$\theta_a = \frac{1}{2}\left[\arccos\left(\frac{M \cos \beta \pi}{c_\gamma\sqrt{1 + c_a^2}}\right) + \arctan(c_a) - \Theta\right]. \tag{3.8}$$

The limiting (non-dimensional) velocities on the leeward (+ superscript) and windward (− superscript) sides of the sheet at the apex are

$$(u_{t,a}^\pm - iu_{n,a}^\pm) = \frac{JP}{2|K|}\left[1 \mp \frac{(1 - iv_a)}{P}\right], \tag{3.9}$$

with $u_{t,a}$ and $u_{n,a}$ being the tangential and normal components relative to the sheet, and P and K are functions of v_a and β, as well as the parameters describing the image system as defined in appendix A. The definitions of the vortex and entrainment sheet strengths are $\gamma = u_t^- - u_t^+$ and $q = u_n^- - u_n^+$, and it can be verified from (3.9) that the strength ratio at the apex satisfies $v_a = q_a/\gamma_a$ as required. Due to the entrainment the flow is no longer stagnated on the leeward side, but instead interacts with that on the windward side to contribute to the forming free sheet.

In the following two sections we will consider certain solutions to the problem outlined above. In § 4, entrainment is limited to the wedge surfaces S_w whereas the free sheet S is a conventional vortex sheet. In § 5, both S_w and S will have non-zero entrainment.

4. Wedge-surface entrainment

In this section we present solutions to (3.5) and (3.6). The numerical approach is essentially the same as Pullin's and inclusion of entrainment does not present any new difficulties in this regard. Hence, the finite-difference forms of the equations have been relegated to appendix B. The current study is limited to the impulsive start with $m = 0$. Pullin showed that $m > 0$ results in a more compact core region with increased ellipticity and a larger fraction of the total circulation in the outer turns of the sheet (i.e. increasingly stronger vorticity is generated at the apex by the acceleration). Here, the presence of entrainment will be limited to the wedge or wall surfaces; entrainment on the free sheet will be discussed in § 5.

4.1. *Validation and large wedge angle results*

As validation, we first reproduced Pullin's results for zero entrainment everywhere on all boundaries: $\nu(\lambda) \equiv 0$ and $\tilde{v}_o = 0$. This corresponds to an image system with $c_\gamma = 1$, $M = 1$ and $\Theta = 0$ (c_q is irrelevant since $\nu = 0$). He was limited by computer storage and thus had a coarser angular resolution of points on the sheet, most particularly near the apex. Using similar spacing we were able to quantitatively obtain his results (his figures 11–13). With the benefit of modern computing, a finer resolution showed that the solutions converge to slightly different values, but which vary only by a few per cent. Some relevant quantities from these latter results are shown in figure 2(*a*). Specifically, the total circulation J and the vortex sheet strength at the apex γ_a are plotted as functions of the wedge apex angle β_a in degrees. The two quantities are related as $\gamma_a = J/|K|$, where K is a complex proportionality constant in the asymptotic solution $\omega = K\lambda$ near the apex (see appendix A) and is also plotted.

Similar to Pullin, we also were not able to obtain converged solutions for $\beta_a > 160°$. This is because the numerical method relies on specification of a unique angular coordinate ϑ for each point on the sheet as measured from the datum line connecting the core point and the wedge apex. The solution for $\beta_a = 160°$ is plotted in figure 2(*b*) and reveals that the datum for ϑ is nearly in line with the tangent direction of the lower wedge face, along which the sheet must shed. For larger wedge angles the ϑ of sheet positions near the apex were no longer unique.

Nevertheless, we may infer the behaviour for $\beta_a \to 180°$ (or $\beta \to 1$) by utilizing the asymptotic solution. In this limit the outer flow approaches a uniform flow. However, the boundary condition at the apex (i.e. the Kutta condition) ensures that a non-zero amount of circulation J will be shed. Rewriting the expressions for γ_a and $|K|$ from appendix A in terms of β, we obtain the following relations for large wedge angles:

$$\gamma_a = c\sqrt{1 - \beta}, \quad J = \frac{c^2(2 - \beta)}{2Q_P}, \quad |K| = \frac{c(2 - \beta)}{2Q_P}\frac{1}{\sqrt{1 - \beta}}. \qquad (4.1a\text{–}c)$$

Here, $c \approx 1.93$ was determined by matching γ_a to the $\beta_a = 160°$ solution. These equations are plotted in figure 2(*a*) as dashed lines. The approximations are quite good for γ_a and $|K|$, appearing continuously differentiable. While there is a 'kink' in the trend for J, the values are reasonable. As $\beta \to 1$ the vortex sheet strength becomes very weak, with $\gamma_a \to 0$ at
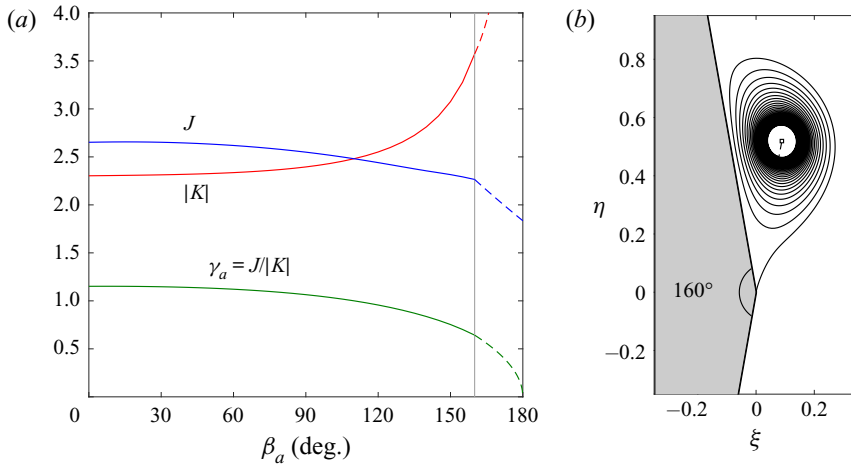
FIGURE 2. Selected numerical results for the baseline case of zero entrainment. (*a*) Variation of non-dimensional solution parameters with wedge angle β_a. The vertical line marks $\beta_a = 160°$ above which numerical solutions were not converged; the dashed lines are approximations for $\beta_a > 160°$ (see text). (*b*) The solution for $\beta_a = 160°$ with 36 resolved turns. The isolated core point vortex (white square) contains 25 % of the total circulation.

the apex, and so the vorticity of total circulation $J \rightarrow 1.86$ becomes more concentrated in the spiral core.

Next, we investigate cases of non-zero entrainment. Our initial interest is in the qualitative effects of entrainment for a given solution. Since the rolled-up spiral shape is topologically similar for all wedge angles (see Pullin's figure 9), we will henceforth focus on the specific wedge angle of $\beta_a = 60°$ corresponding to $n = 0.6$.

4.2. *Some new vortex sheet solutions*

As discussed in § 2, a unique solution for a given $\tilde{\nu}_o = Q_o/\Gamma_o$ requires that we specify the functional distribution of the strength ratio $\nu(\lambda)$ along the free sheet. This clearly represents a considerable amount of freedom, in fact, an infinite amount. With this in mind, we recall that the conventional vortex sheet, which has proven to be a valuable model, is a special case having $\nu \equiv 0$ on the sheet. For our current problem there are actually additional vortex sheet solutions other than those found by Pullin and we now consider these possibilities. There are two main physical implications, the first being the usual inviscid fluid assumption such that vorticity is not diffused from the free sheet. Consequently, any entrainment must occur on the wall-bound sheets and represents the effect of the no-slip condition on the solid wedge surfaces in a viscous fluid. There is no intuitive meaning to the image system other than when it satisfies a desired boundary condition (e.g. the wedge is a streamline or zero entrainment at infinity). To this end, we endeavour to stray as little as possible from Pullin's situation by taking $c_\gamma = 1$ and $\tilde{\nu}_o = 0$ (again c_q is irrelevant here). Since $\nu \equiv 0$, then we have technically imposed $\tilde{\nu}_s = 0$, or $Q_s = 0$ rather, and so a degree of freedom is lost. This means that for each M there is a unique value of Θ, which is now to be found as part of the solution rather than given.

From (2.8*a*,*b*) we find that $\Gamma_\infty = 0$ and $Q_\infty = 0$, and subsequently from (2.7*a*,*b*) that $\Gamma_s = -\Gamma_w$ and $Q_w = 0$. Recall that these circulations and entrainments are those due to the velocity induced by just the free sheet (i.e. excluding the driving flow). Therefore, the
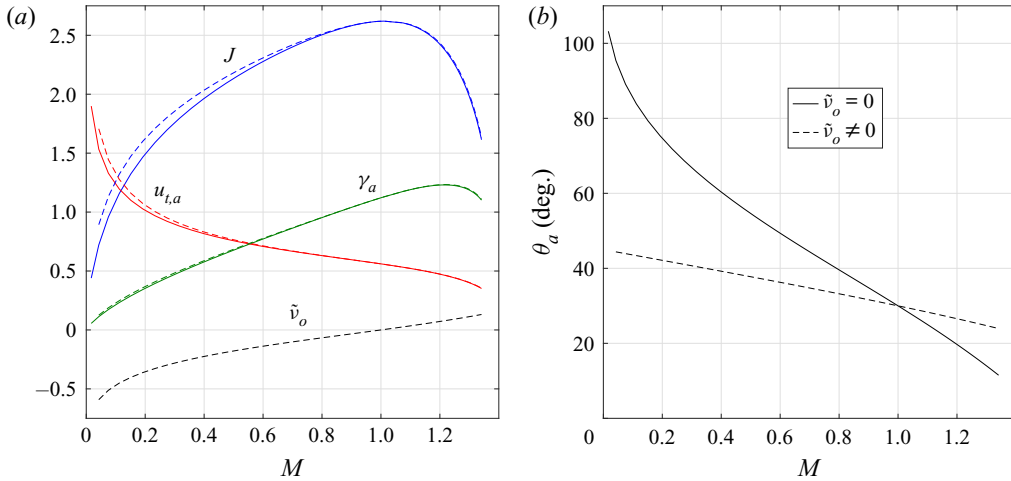
FIGURE 3. Results for two solution sets with a conventional vortex sheet S in the fluid, but non-zero local entrainment on S_w the wedge surfaces. $\tilde{v}_o = 0$ (solid lines); $\tilde{v}_o \neq 0$ (dashed lines), where $\tilde{v}_o = Q_o/\Gamma_o$ is the boundary condition at infinity. M is the scaling factor in the image system. (*a*) Total circulation J, vortex sheet strength γ_a and shedding velocity $u_{t,a}$ at the apex. (*b*) The shedding angle θ_a. The baseline case of Pullin is $M = 1$ with $\theta_a = \beta_a/2 = 30°$.

circulation in the free sheet will be equal and opposite to that which it induces on the wedge. While the net entrainment from the walls is zero, there is a non-zero local flux at any given point; since $\tilde{v}_o = 0$ the driving flow, being everywhere tangent to the wedge, has no contribution to this local entrainment.

By the requirements in appendix A, there is a finite range $0 < M < M_{max}$, which here is limited by $M_{max} = 1/|\cos \beta \pi| = 2$. In the numerical set-up we varied M within this range and the scheme solved for the corresponding unique Θ value. For comparison, another related set of solutions is obtained in a similar fashion. Namely, the effect of a non-zero flux at infinity due to the driving flow is included by allowing $Q_o \neq 0$, this flow now having a component normal to the wedge boundary. Equivalently, $\tilde{v}_o \neq 0$ and its unique value corresponding to a specified M is now the quantity to be obtained from the solution, thus replacing Θ which is returned to the fixed value $\Theta = 0$ of the baseline case. Both solution sets will now be discussed.

Figure 3(*a*) plots J, γ_a, and the shedding velocity at the apex $u_{t,a}$, each as a function of M; above $M \approx 1.35$ the system became very 'stiff' and solutions no longer converged. The results are remarkably similar, despite different boundary conditions at infinity, being essentially identical for $M > 1$ and only a slight diverging for $M < 1$. For the cases with $\tilde{v}_o \neq 0$, this quantity is also plotted and reveals that $(M - 1)$ and $\tilde{v}_o$ have the same sign. This allows us to infer that the effect of the image system for the $\tilde{v}_o = 0$ cases is to nearly preserve the plotted quantities. Moreover, recalling that $\tilde{v}_o = -U_n/U_t$, we can then interpret this quantity as a measure of a 'streamwise' flow component, with $\tilde{v}_o < 0$ meaning flow away from the wall and $\tilde{v}_o > 0$ toward the wall. The direction of the flow relative to the apex then explains why the total circulation J decreases from the baseline for all cases, as well as the simultaneous increase/decrease of γ_a with $\tilde{v}_o$. However, the solutions display significant differences in the sheet position. For example, figure 3(*b*) plots the shedding angle θ_a vs. M for the two sets. While θ_a increases/decreases away from the wedge tangent ($\theta_a = \beta_a/2 = 30°$) of the baseline case for both sets, the corresponding
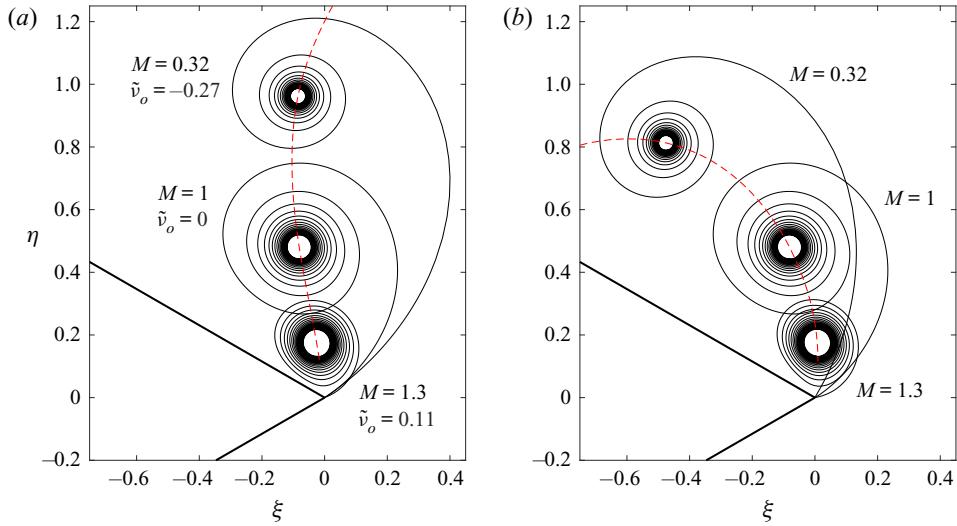
FIGURE 4. Sheet shapes for the two solution sets described in figure 3 with different boundary conditions at infinity $\tilde{\nu}_o$ as labelled. The dashed red line is the trajectory of the core point as M, the image system scaling, is continuously varied. $M = 1$ is the baseline case of Pullin. (*a*) $\tilde{\nu}_o = Q_o/\Gamma_o \neq 0$ and (*b*) $\tilde{\nu}_o = Q_o/\Gamma_o = 0$.

rates are considerably different. The differences are best observed from the sheet positions as shown in figure 4. Also shown is the trajectory of the isolated core point. When the 'streamwise' flow is away from the wall ($\tilde{\nu}_o < 0$) the core is convected downstream thus elongating the arclength of the outermost turn that connects to the apex. Conversely, when this flow is toward the wall ($\tilde{\nu}_o > 0$), the overall sheet size shrinks toward the apex with the outer turns becoming much closer. When $\tilde{\nu}_o = 0$ the same features occur, but the core trajectory encroaches further along the upper wedge surface, as expected from the dominant tangential flow around the apex.

The amount of circulation contained in the sheet (not shown) was also the same between the two solution sets. This amount changed significantly with M, however, decreasing from about 90 % at $M \ll 1$ to almost 40 % at $M = 1.3$; for each case 20 turns were resolved. Paired with the observed changes in the size/diameter of the unresolved core region, this indicates that the vorticity distributions in the spiral correspondingly shift from very compact to more diffused or spread. We will revisit this interpretation in more detail in § 5.1.

4.3. *Comparison with experiment*

Next, we compare some similarity solutions to the experiments of Pullin & Perry (1980). For the case that we have investigated here ($\beta_a = 60°$ and $m = 0$), they report significant deviations of the rolled-up core position as compared to the similarity theory of Pullin (1978); see table 1. We first note that in the experiments the boundary condition at 'infinity' was a uniform flow rather than (2.6) as used here and in Pullin's work; additionally the wedge height was nearly half the water tunnel height. This most certainly affects the development of the shedding shear layer, particularly at larger times, but at small times Pullin & Perry (1980) claim the discrepancies are attributable to viscous or finite Reynolds number effects. The implication is that at early times secondary effects are negligible so that the tangential flow around the apex dominates and we assume that $\tilde{\nu}_o = 0$ is the
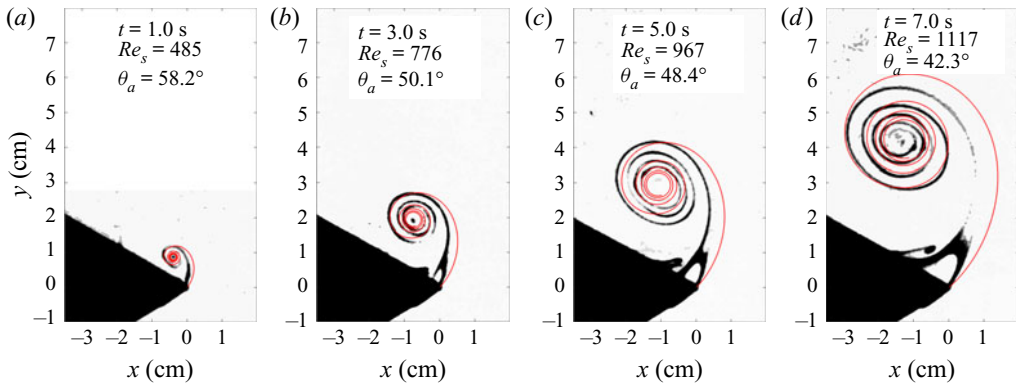
FIGURE 5. Comparison with the dye visualization experiments of Pullin & Perry (1980); images adapted from their figure 5. The similarity sheet shapes (red lines) were matched and converted to the dimensional space by finding the value of M for which the experimental core position aligned with that of the predicted trajectory. The value of M corresponds to a unique value of the shedding angle θ_a as labelled.

	$t \approx 0.5$ s	$t \approx 1.4$ s	$t \approx 3.0$ s	$t \approx 5.0$ s
x-coord. error	190 %	170 %	150 %	140 %
y-coord. error	4.5 %	10 %	12 %	20 %

TABLE 1. Approximate errors between the similarity prediction of Pullin and the experiments of Pullin & Perry (1980) for the x- and y-coordinates of the core position. Much larger errors in the x-coordinate are due to the experimental measurement itself being a small quantity.

appropriate boundary condition at infinity. We recall from § 4.2 that this corresponds to local entrainment on the wedge surfaces, which we interpret as the viscous entrainment of the boundary layers in the experiment. The infinite wedge problem has no physical length scale, but by dimensional analysis an implicit length scale can be defined. This was used by Pullin & Perry (1980) to define the 'scale Reynolds number' Re_s, which can also be interpreted as a non-dimensional time for the growth of the spiral structure. Figure 5 shows some of their dye visualization images at several different Re_s values. Note that the apparent shedding angle is 'kinked' well past/above the wedge tangent direction. This feature is shared by the similarity solutions presented in figure 4(*b*) with shedding angles in figure 3(*b*). A non-tangential shedding angle requires non-zero entrainment at the apex.

To make comparison to the experiment using a solution from the current study, the measurements of the core position from Pullin & Perry (1980) were converted to our similarity space (we note the absorption of the constant C from (3.3) in their definition of ω). The values were then compared to the core trajectory in figure 4(*b*). It was found that one experimental case intersected the curve and the corresponding solution was transformed to physical space by scaling to the core location. The result is shown in figure 5(*d*) and exhibits fair agreement considering the somewhat crude assumptions made above about the boundary condition at infinity. However, the experimental shedding angle is still noticeably larger than the predicted one.
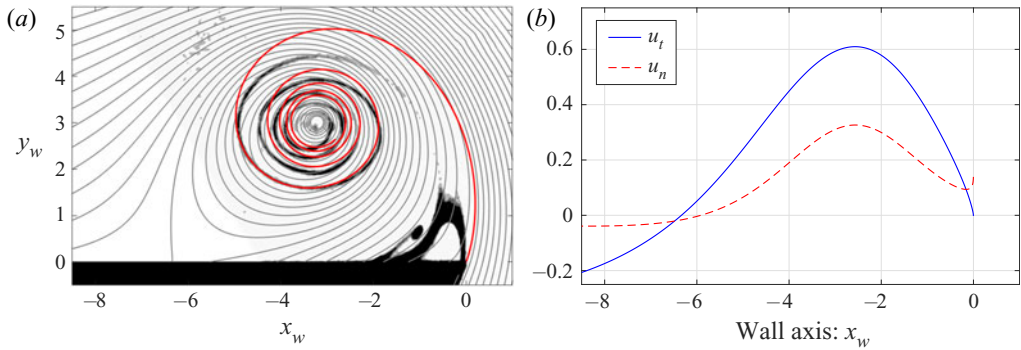
FIGURE 6. More similarity results for the case in figure 5(*d*). The $x_w - y_w$ axes are a right-handed coordinate system on the surface; the scaling was arbitrarily chosen. (*a*) Overlaid streamlines of inviscid flow (grey lines). (*b*) Non-dimensional velocities on the upper wall surface: u_t, tangent component (solid blue); u_n, normal component (dashed red).

Images of the flow development at three earlier times are shown in figure 5(*a–c*). According to the similarity growth law, for constant parameters the core trajectory in the physical domain follows a constant-angle ray as time increases. This behaviour is clearly not obeyed in the early growth of the spiral. Hence, there must be some other time-dependent effect present in the experiments. We now recall the comments immediately following (3.6) about an implicit time scale that may occur if a time-dependent value is prescribed for any of the input parameters defining the self-similar problem. Figure 5 indicates that this implicit effect manifests as a time-dependent shedding angle θ_a at the apex, which is noted as part of the boundary. By (3.8) we can affect a time-dependent shedding angle through different values of the image system scaling $M(t) \leftrightarrow \theta_a(t)$. Therefore, we can identify similarity solutions representative of other experimental times by tracing the ray that passes through both the measurement point and the trajectory curve, and again scaling to the core location. The results are overlaid in figure 5(*a–c*) and also show fair agreement.

The features of the flow (e.g. shedding angle, core location) are naturally dictated by the boundary conditions. In the experiment, the actual time-dependence and functional connection between these quantities is a more complicated state of affairs. For instance, it is difficult to ascertain the effects, both quantitative and qualitative, of the finite tunnel dimensions or the far-field flow without being given more detailed information. Two physically impactful examples from the experiment are the appearance, near the apex, of a secondary roll-up due to boundary layer separation on the upper wedge face and a corresponding recirculating region, both of opposite sign to the primary separation. Figure 6(*a*) reproduces the plot of figure 5(*d*), but with the streamlines of the inviscid flow overlaid. The axes are rotated so that the leeward face is horizontal. The inviscid flow emanates out from the wedge surface, qualitatively capturing the displacement effect of the viscous boundary layer. Figure 6(*b*) plots the wall-tangential and wall-normal velocity components along the wedge surface. By potential theory, the pressure minimum and velocity maximum must each be located somewhere on the boundary. Moreover, in the similarity space the flow appears steady so that $(p - p_o) \sim -(u_t^2 + u_n^2)$ and these two points coincide. Hence, the separation is correctly placed between the predicted pressure minimum and the apex, occurring almost immediately downstream of the former; see the discussion in Pullin & Perry (1980) on page 248 for more. While these results support the ability of the vortex-entrainment sheet model to capture viscous effects, it is noteworthy

that the secondary separation bubble is a topological feature that is not possible with the current problem set-up. We believe that proper modelling of this phenomenon ought to involve boundary conditions other than those offered by (2.6) as used presently.

5. Entrainment on the free sheet

Having investigated entrainment solely on the wedge surfaces in § 4, we now present solutions for which the strength ratio distribution on the free sheet is given by a simple function $\nu(\lambda)$. The image system is defined by $c_\gamma = 1$, $c_q = 1$, $M = 1$, and $\Theta = 0$, which corresponds to the standard 'mirror image'. From (2.8a,b) and (2.7a,b), we have $\Gamma_s = -\Gamma_w$ and $Q_s = -Q_w$. The problem is then closed upon specification of $\tilde{v}_o$ and gives the unique outputs J, $\tilde{v}_s$, and ω. From the results, we will infer some further plausible physical connections between entrainment and viscous effects.

The convergence of the scheme was mostly dependent upon the number of turns resolved in the sheet and thus the (fractional) amount of circulation λ_c contained in those turns. However, global output parameters were remarkably insensitive to λ_c so long as the first few turns are present. The computational purchase of resolving more turns is the local structure of the sheet shape near the core region. As will be seen below, sheet entrainment eventually brings a given number of turns much closer to the isolated core point. For numerical stability $\tilde{v}_o$ was treated as the unknown and $\tilde{v}_s$ was specified instead (see appendix B). Solutions were obtained by incrementing $\tilde{v}_s$, using the previous solution as an initial condition. The step in $\tilde{v}_s$ was throttled so that the corresponding change in λ_c was approximately 1 % of the total circulation.

5.1. *Core entrainment*

Here, the form of the strength ratio on the sheet is designed so that the entrainment is concentrated toward the spiral core of the sheet, namely

$$\nu(\lambda) = a\lambda^p, \tag{5.1}$$

and note that $a = (1 + p)\tilde{v}_s$, where the exponent p is a parameter that controls the size of the region within which the entrainment is appreciable. Also, since $\nu_a = \nu(0) = 0$ at the apex, then by (3.8) the shedding angle remains tangential to the lower wedge face.

Figure 7(a) plots $\tilde{v}_s$ against $\tilde{v}_o$ for $p = 1$, 2, and 5. This plot may essentially be interpreted as a measure of the net sheet entrainment vs. the flux at infinity. For $\tilde{v}_s < 0$ the relationship is almost perfectly linear with slope approximately equal to $\tilde{v}_s/\tilde{v}_o \approx 3/2$, independent of p. For $\tilde{v}_s > 0$ the slope gradually approaches a constant, but which depends on p. Below it is shown that as $\tilde{v}_s > 0$ increases, the amount of circulation in the isolated core also increases (or that in the sheet decreases). Moreover, approximately 50 % of this circulation resides within a very small radius around the core. By approximating this portion of the sheet with the single core point, the relationship $\tilde{v}_s/\tilde{v}_o \sim (1 + p)^{-1}$ can be inferred from the Kutta conditions in (3.6).

Next, we recall that $\tilde{v}_s < 0$ corresponds to flow exiting the sheet, while $\tilde{v}_s > 0$ represents flow entering the sheet. Hence, for this problem set-up, there is a respective efflux and influx of fluid across the boundary C_∞ at infinity since $\tilde{v}_o$ shares the same sign. A similar phenomenon occurs for Falkner–Skan boundary layers, whereby the vertical flow at infinity changes from an efflux to an influx as the outer flow acceleration is increased, which competes with the displacement of the layer growth due to diffusion (see DeVoria & Mohseni 2019). Motivated by this, we label $\tilde{v}_s < 0$ as 'diffusion-dominated entrainment' (DDE) and $\tilde{v}_s > 0$ as 'inertia-dominated entrainment' (IDE). To give credence to these
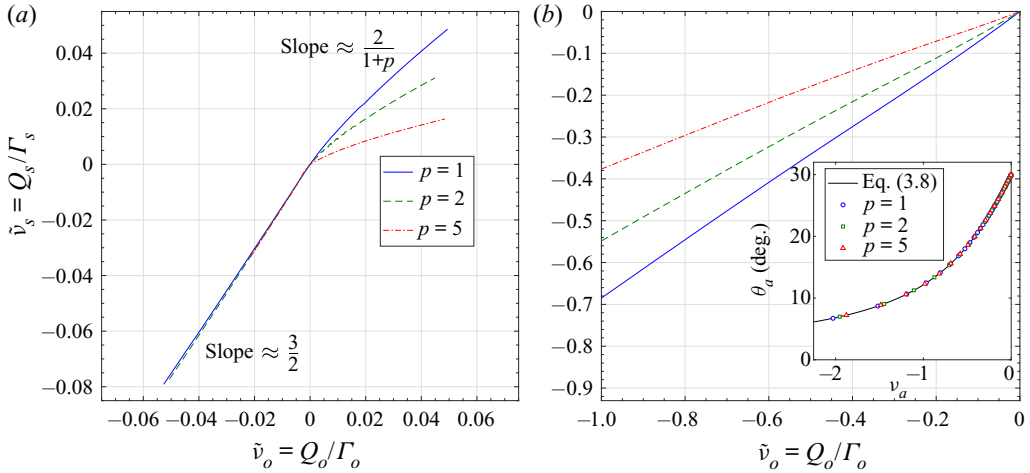
FIGURE 7. The average strength ratio on the sheet $\tilde{\nu}_s = Q_s/\Gamma_s$ vs. the boundary condition at infinity $\tilde{\nu}_o = Q_o/\Gamma_o$. (a) Core entrainment with the $\nu(\lambda)$ distribution given by (5.1). (b) Apex entrainment with the $\nu(\lambda)$ distribution given by (5.2). The inset plots the shedding angle θ_a vs. the strength ratio at the apex $\nu_a = \nu(0)$; the line is the asymptotic theory while symbols are directly measured from the numerical solutions.

assignments, figure 8(*a*–*f*) plots several examples for each entrainment type with $p = 1$ as the exponent in (5.1); the baseline case of $\tilde{\nu}_s = 0$ is shown in figure 8(*d*). For DDE the outer turns of the spiral gradually spread outward, while the inner most turns concentrate much closer toward the isolated core point. Moreover, as indicated in each panel, the circulation contained in the resolved sheet λ_c rapidly increases, reaching 99.9 % at $\tilde{\nu}_s = -0.035$; all cases maintained 20 turns. As such, the effect of the core point is negligible as its circulation has been almost entirely redistributed or spread out along the sheet. The total circulation J increased/decreased with $\tilde{\nu}_s$ by less than 1 % over the range shown in the figure. The IDE cases have an opposing trend with circulation being transported from the sheet to the core point with fractional circulation $(1 - \lambda_c)$. Consequently, the spiral is drawn closer to the core point owing to its sink-like entrainment. However, the turns maintain their tightly wound spacing and also become more circular with any ellipticity practically vanishing. In general, while there is a significant change in the spacing of the turns, the large-scale dimensions and position of the core point are essentially unaffected for all cases.

The features in figure 8 may be readily interpreted through a relevant aerodynamic application, namely the spanwise flow often observed in leading-edge vortices. This phenomenon has been thought to be a stabilizing mechanism in rotating wing lift generation (e.g. Ellington *et al.* 1996). Here, this flow would be out-of-plane and IDE would correspond to removal of in-plane fluid (stabilizing), while DDE injects fluid into the plane due to a decelerating spanwise flow causing growth of the vortex.

5.2. *Apex entrainment*

In this section we give a similar analysis for a strength ratio that concentrates the entrainment near the apex, namely

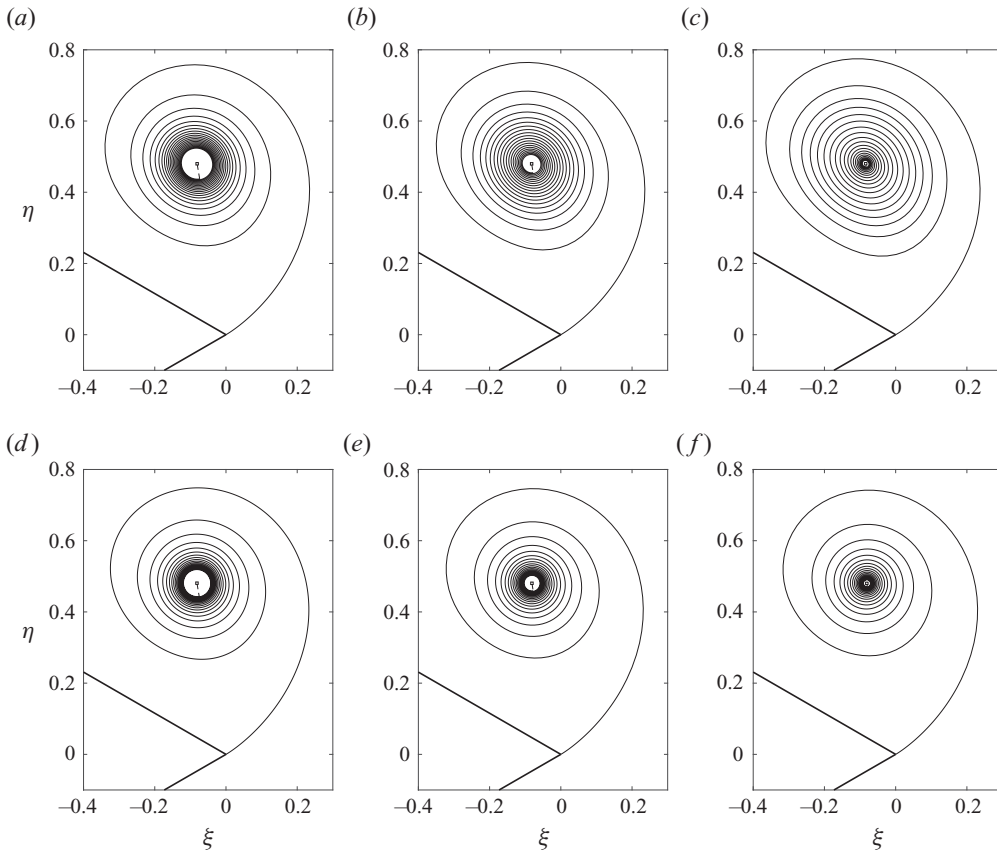$$\nu(\lambda) = a(1 - \lambda)^p. \tag{5.2}$$

FIGURE 8. Self-similar sheet shapes with entrainment concentrated near the core region. The strength ratio is given by (5.1) with $p = 1$. (*a*–*c*) Diffusion-dominated entrainment: $\tilde{\nu}_s < 0$. (*d*–*f*) Inertia-dominated entrainment: $\tilde{\nu}_s \geq 0$; (*d*) is the baseline case. Each case has 20 resolved turns and λ_c is the fraction of the total circulation contained in these turns. (*a*) $\tilde{\nu}_s = -0.013$, $\lambda_c = 0.952$, (*b*) $\tilde{\nu}_s = -0.022$, $\lambda_c = 0.991$, (*c*) $\tilde{\nu}_s = -0.035$, $\lambda_c = 0.999$, (*d*) $\tilde{\nu}_s = 0$, $\lambda_c = 0.752$, (*e*) $\tilde{\nu}_s = 0.005$, $\lambda_c = 0.650$ and (*f*) $\tilde{\nu}_s = 0.010$, $\lambda_c = 0.562$.

Again we have $a = (1 + p)\tilde{\nu}_s$ and this is also equal to the strength ratio at the apex ν_a. Figure 7(*b*) plots the corresponding $\tilde{\nu}_s$ vs. $\tilde{\nu}_o$ for different values of p. Some solutions for small positive values of $\tilde{\nu}_o$ were obtained, but the iterative solver soon became extremely slow to converge. Moreover, it was evident that the sheet shape at the apex did not agree with the shedding angle given by (3.8). We concluded, then, that the boundary conditions for this particular self-similar problem do not admit solutions for $\tilde{\nu}_o > 0$ when the entrainment is non-zero at the apex.

For $\tilde{\nu}_o < 0$ we again see a linear relationship to $\tilde{\nu}_s$ and with a slope that depends on p. Since the entrainment is concentrated at the apex, the inner structure of the spiral remains relatively unchanged, whereas the orientation of the spiral and the core point location are drastically altered. For instance, the variable shedding angle is plotted vs. the strength ratio at the apex as the inset of figure 7(*b*). Both direct measurements of θ_a from the sheet shape and (3.8) are shown, thus further validating the asymptotic theory. Again adopting the label DDE for $\tilde{\nu}_s < 0$, we see that the 'diffusion' near the apex results in θ_a approaching the wedge bisector. The larger magnitudes of $\tilde{\nu}_o = -U_n/U_t$ compared to § 5.1 occur because,
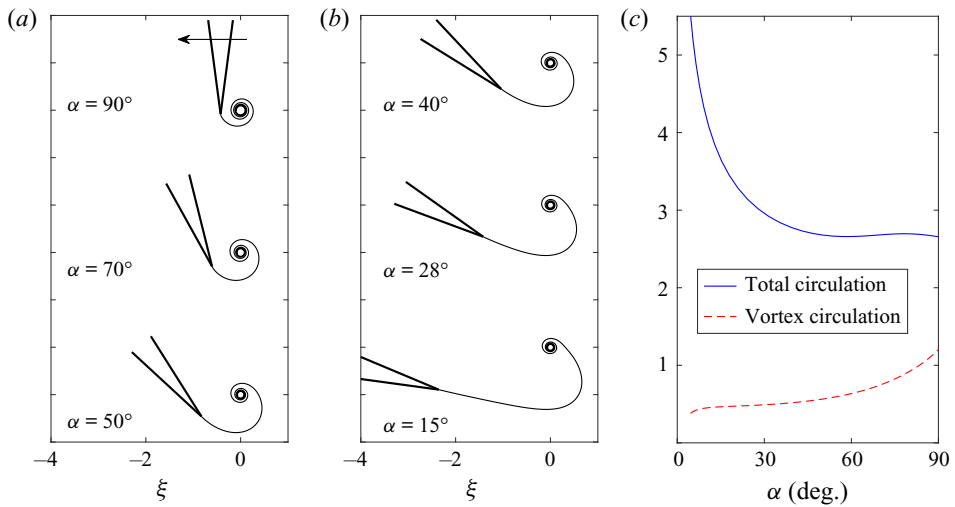
FIGURE 9. (*a*,*b*) Examples of the airfoil analogy with trailing-edge separation. The motion is a leftward surge at angle of attack $\alpha = \pi/2 + \arctan(\tilde{v}_o)$ measured from the horizontal to the wedge bisector (i.e. chord line). The wedge angle is $\beta_a = 15°$. (*c*) The total circulation in the sheet (solid blue) and the isolated vortex circulation (dashed red) as functions of α.

below a certain value, the core structure essentially convects downstream while remaining connected to the apex by a long 'umbilical'. Although the physical flow at infinity is not uniform, we may draw a qualitative analogy with the angle of attack of an airfoil. For our chosen orientation of the wedge geometry, the U_t component represents a vertical plunge, while U_n represents a streamwise component. Therefore, we can rotate our reference to define an angle of attack as $\alpha = \pi/2 + \arctan(\tilde{v}_o)$ so that the motion corresponds to a leftward surge of the 'airfoil' at angle of attack α relative to the horizontal.

To illustrate this concept, we computed solutions for a $\beta_a = 15°$ wedge representing a thin, but finite-angled trailing edge. The exponent value $p = 5$ was chosen so that the sheet entrainment was restricted to the apex region. Figure 9(*a*,*b*) plot a series of such solutions, where again the angle of attack α is measured from the horizontal to the wedge bisector or chord line. As α decreases, the size of the rolled-up core appears to decrease. Figure 9(*c*) plots the total circulation in the sheet J along with the circulation contained in the isolated core vortex $J(1 - \lambda_c)$. The latter quantity depends on the number of resolved turns, however, this was the same for each case (five turns). The vortex circulation decreases with α, indicating a weaker starting vortex at lower angles of attack. Conversely, the total circulation increases as α decreases, but this corresponds to the longer arclength of the shed sheet. For $\alpha \to 0$, these results indicate that the umbilical sheet is infinitely long and the starting vortex core is at infinity, which agrees with Prandtl's classical aerodynamics description of steady lift. However, the vorticity of infinite total circulation ($J \to \infty$) is distributed along the sheet with a vanishingly weak starting vortex, which is similar to Wagner's lift development.

6. Conclusion

Building off previous work by the authors, this paper explored the potential to capture viscous flow effects using an inviscid model with singular sheets of discontinuity taking the place of the actual viscous layers. The case study used was starting flow separation

over a sharp wedge. Specifically, the self-similar solutions originally computed by Pullin (1978) were significantly augmented by including entrainment. This was accomplished by consideration of a broader class of boundary conditions for the problem. The specification of these conditions is tantamount to supplying the entrainment. This is a consequence associated with foregoing a fluid description whose governing equation is able to accommodate more independent boundary conditions.

Mass flux into the boundaries, represented as vortex-entrainment sheets, is allowed by relaxing the usual, yet axiomatically assumed normal boundary condition of no through flow. This mass entrainment offers a more thorough dynamical inviscid model which, in particular, is argued to represent viscous effects. For example, global quantities, such as the total circulation, as well as local quantities, such as the shedding angle, sheet strength and velocity at the apex, may all be manipulated through the entrainment. Several computed solutions were presented and showed favourable agreement with an existing experimental work. Moreover, some phenomena in the experiment attributed to viscous effects were captured, qualitatively at the very least, by the inviscid model. When the entrainment was specified on the freely shed sheet, some familiar features commonly encountered in aerodynamic applications were observed. It was argued that the displacement effect/velocity of a thickening layer is represented by 'diffusion-dominated entrainment', for which mass/fluid emanates out of the sheet. In a similar manner, a sink-like flow into the sheet corresponds to 'inertia-dominated entrainment', for which large accelerations or fast velocities generate strong vorticity. Consequently, the vorticity becomes increasingly concentrated within a tightly wound spiral core.

As a whole, we interpret the model features to be the representation of a finite Reynolds number. Of course, the fidelity of the inviscid results depends on the level of information contained in the entrainment boundary condition. Ideally, the local entrainment function would correspond to that of the actual boundary layers. However, we likely will not be given this detailed distribution *a priori*, but instead will have certain global quantities that must be satisfied on physical grounds for a certain problem, such as a net force, the rate of mass consumption or energy dissipation. In turn, these quantities could be used to determine some of the free parameters in the present model, such as the averaged strength ratio for a given sheet. This is an ideal task for future work. Other relevant studies may focus on practical applications, such as flow control devices for manipulation of fluid–structure interactions. Here, entrainment from solid surfaces can be directly imposed through mechanisms injecting/suctioning mass into/from the fluid.

Acknowledgements

Declaration of interests

The authors report no conflict of interest.

Appendix A. Asymptotic solution near the apex

In this appendix the asymptotic solution for $\omega(\lambda) \to 0$ (with $\lambda \to 0$) is given. This analytically determines the shedding angle of the free sheet as well as the strengths of the vortex and entrainment sheets at the apex: γ_a and q_a. The results are not specific to the assumed forms of $\nu(\lambda)$ used above and thus are applicable to arbitrary strength ratios.

Moreover, while we use the non-dimensional self-similar equations in § 3 to proceed here, the same basic analysis is valid on the general equations of § 2.

Using the vector Kutta condition in (3.6), we can rewrite (3.5) as

$$(1-n)\left[\bar{\omega} + Q_P(1-\lambda)\frac{d\bar{\omega}}{d\lambda}\right] = nJ\omega^{2n-1}G(\omega), \tag{A 1}$$

where the function $G(\omega)$ is defined similar to that in Pullin as

$$G(\omega) = \frac{1}{2\pi i}\int_0^1\left[\frac{1-i\nu(\lambda')}{\omega'^n(\omega^n - \omega'^n)} + \frac{c_\gamma - ic_q\nu(\lambda')}{\bar{A}^n\omega'^n(\omega^n + \overline{A^n\omega'^n})}\right]d\lambda'. \tag{A 2}$$

Next, take $\omega = K\lambda^\mu$ where $K = |K|\,\mathrm{e}^{i\theta_a}$ and θ_a is the argument of an infinitesimal length of the sheet at the apex measured anticlockwise positive from the wedge bisector and thus is the shedding angle. With this form of $\omega(\lambda)$ the behaviour of the $G(\omega)$ integral as $\omega \to 0$ can be obtained from Muskhelishvili (1946). Upon substitution into (A 1) it can be shown that $\mu = 1$ to match leading orders of λ, and subsequently that

$$|K|^2 = \frac{J}{2(1-n)Q_P}\left\{\frac{\bar{A}(1-i\nu_a)\cos\beta\pi - (c_\gamma - ic_q\nu_a)\,\mathrm{e}^{i2\theta_a}}{-i\bar{A}\sin\beta\pi}\right\}, \tag{A 3}$$

where $\nu_a = \nu(0)$ is the value of the strength ratio at the apex. The term in curly brackets, say P, must then be purely real, which determines the shedding angle as

$$\theta_a = \pm\frac{1}{2}\left[\arccos\left(\frac{M\cos\beta\pi}{c_\gamma\sqrt{1+c_a^2}}\right) + \arctan(c_a) - \Theta\right], \tag{A 4}$$

where $(\pm) = \mathrm{sgn}(U_t)$, $c_a = c_q\nu_a/c_\gamma$ and recall that $A = M\,\mathrm{e}^{i\Theta}$. Then $P \in \mathbb{R}$ is given by

$$P = \frac{\nu_a\cos\beta\pi + c_\gamma\sqrt{(1+c_a^2)/M^2 - (\cos^2\beta\pi)/c_\gamma^2}}{\sin\beta\pi}. \tag{A 5}$$

That P remains real and strictly positive gives obvious restrictions on the parameters involved. In particular, $0 < M < M_{max}$ where $M_{max}^2 = (c_\gamma^2 + c_q^2\nu_a^2)/\cos^2\beta\pi$. Next, we have

$$G(\omega) = \frac{\omega^{1-2n}P}{2nK} + G^*(\omega), \quad |K| = \left[\frac{JP}{2(1-n)Q_P}\right]^{1/2}, \tag{A 6a,b}$$

where $\omega^{2n-1}G^*(\omega) \to 0$ as $\omega \to 0$. The Plemelj formulae give the complex velocities on the leeward $(+)$ and windward $(-)$ sides of the sheet at the apex for $U_t > 0$ as

$$\left.\frac{d\Omega^\pm}{d\omega}\right|_{\omega=0} = (u_{t,a}^\pm - iu_{n,a}^\pm) = \frac{JP}{2|K|}\left[1 \mp \frac{1-i\nu_a}{P}\right], \tag{A 7}$$

where $u_{t,a}$ and $u_{n,a}$ are, respectively, the tangential and normal components relative to the sheet. By definition, the strengths of the vortex and entrainment sheets are

$$\gamma_a = u_{t,a}^- - u_{t,a}^+ = \frac{J}{|K|}, \quad q_a = u_{n,a}^- - u_{n,a}^+ = \nu_a\frac{J}{|K|}, \tag{A 8a,b}$$

and thus $q_a/\gamma_a = v_a$ as required. Likewise, the sheet velocities (i.e. principal value) are

$$u_{t,a} = \frac{1}{2}(u_{t,a}^+ + u_{t,a}^-) = \frac{JP}{2|K|}, \quad u_{n,a} = \tfrac{1}{2}(u_{n,a}^+ + u_{n,a}^-) = 0. \quad\quad (A\,9a,b)$$

For $U_t < 0$ the ($\mp$) in (A 7) is simply inverted to ($\pm$), which changes the signs of θ_a and $\gamma_a = u_{t,a}^- - u_{t,a}^+$ from positive to negative, while the entrainment $q_a = u_{n,a}^- - u_{n,a}^+$ takes a sign in accordance with $q_a = v_a \gamma_a$.

Appendix B. Numerical scheme

Here, we detail the method used by Pullin along with the modifications required to include entrainment. The reader is referred to his paper for additional information.

The sheet is represented by $k = 1, \ldots, N$ planar segments with circulation $\lambda_{k-1} < \lambda \le \lambda_k$ and with endpoints ω_{k-1} and ω_k. The isolated point singularity is located at $\omega_{N+1} = \omega_c = r_c\,e^{i\theta_c}$ with net strength $J(1 - \lambda_N)(1 - i\tilde{v}_c)$ where $\lambda_N = \lambda_c$ and $\omega_N = \omega_s$. Finite difference versions of (3.5) are solved at the midpoints defined as

$$\omega_{k-1,k} = \tfrac{1}{2}(\omega_{k-1} + \omega_k), \quad \lambda_{k-1,k} = \tfrac{1}{2}(\lambda_{k-1} + \lambda_k) \quad \{k = 1, \ldots, N\}. \quad\quad (B\,1a,b)$$

The derivative $d\bar{\omega}/d\lambda$ is computed with a central difference and all integration is performed with the trapezoidal rule. As such, the system (3.5)–(3.7) can be written as

$$
\left.
\begin{aligned}
0 &= (1-n)\left[\bar{\omega}_{k-1,k} + Q_P(1 - \lambda_{k-1,k})\left(\frac{\bar{\omega}_k - \bar{\omega}_{k-1}}{\lambda_k - \lambda_{k-1}}\right)\right] \\
&\quad + in(\omega_{k-1,k})^{n-1}\left\{(1 - i\tilde{v}_o) + \frac{J}{2\pi}\sum_{j=0}^{N+1} F_j(\omega_{k-1,k})A_j\right\}, \\[2mm]
0 &= \left\{(1 - i\tilde{v}_o) - \frac{J}{2\pi}\sum_{j=0}^{N+1}\left(H_j^\gamma B_j - iH_j^q C_j\right)\right\}, \\[2mm]
0 &= (1-n)\left[\bar{\omega}_{N+1} + Q_P\left(\frac{\bar{\omega}_{N+1} - \bar{\omega}_N}{1 - iv_{N+1}}\right)\right] + in(\omega_{N+1})^{n-1}\left\{(1 - i\tilde{v}_o) + \frac{J}{2\pi}\sum_{j=0}^{N+1} G_j A_j\right\},
\end{aligned}
\right\}
$$
$$(B\,2)$$

with $Q_P = (n + 2m)/(1 + m)$ and

$$
\left.
\begin{aligned}
F_j(\omega_{k-1,k}) &= \left[\frac{1 - iv_j}{\omega_{k-1,k}^n - \omega_j^n} + \frac{-(c_\gamma - ic_q v_j)}{\omega_{k-1,k}^n + \overline{A^n \omega_j^n}}\right], \\[2mm]
v_j &= v(\lambda_j), \quad v_{N+1} = \tilde{v}_c = \frac{1}{1 - \lambda_N}\int_{\lambda_N}^1 v(\lambda)\,d\lambda, \\[2mm]
G_j &= F_j(\omega_{N+1}), \quad G_{N+1} = \left[\frac{-(c_\gamma - ic_q v_{N+1})}{\omega_{N+1}^n + \overline{A^n \omega_{N+1}^n}} + \frac{(n-1)(1 - iv_{N+1})}{2n\omega_{N+1}^n}\right], \\[2mm]
H_0^\gamma &= H_1^\gamma, \quad H_0^q = H_1^q, \quad H_j^\gamma = \frac{\overline{A^n \omega_j^n} + c_\gamma \omega_j^n}{\overline{A^n |\omega_j^n|^2}}, \quad H_j^q = \frac{\overline{A^n \omega_j^n} + c_q \omega_j^n}{\overline{A^n |\omega_j^n|^2}},
\end{aligned}
\right\}
$$
$$(B\,3)$$

where the two terms in G_{N+1} are the velocities due to the image of the isolated point singularity and the Routh correction $(f''/2(f')^2$ where $f(z) = z^n)$, respectively, and

$$
\left.
\begin{aligned}
A_0 &= \tfrac{1}{2}(\lambda_1 - \lambda_0), \quad A_N = \tfrac{1}{2}(\lambda_N - \lambda_{N-1}), \quad A_{N+1} = 1 - \lambda_N, \\
A_j &= \tfrac{1}{2}(\lambda_{j+1} - \lambda_{j-1}) \quad \{j = 1, \ldots, N-1\}, \\
B_0 &= \frac{\lambda_1}{1-n}, \quad B_1 = \tfrac{1}{2}(\lambda_2 - \lambda_1), \quad B_j = A_j \quad \{j = 2, \ldots, N+1\}, \\
C_0 &= \lambda_1^n \int_0^{\lambda_1} \frac{\nu(\lambda)}{\lambda^n} \, \mathrm{d}\lambda, \quad C_j = B_j \nu_j \quad \{j = 1, \ldots, N+1\}.
\end{aligned}
\right\}
\tag{B 4}
$$

The C_0 term and the average $\nu_{N+1} = \tilde{\nu}_c$ each depend on the strength ratio distribution $\nu(\lambda)$. For the two cases of (5.1) and (5.2) studied in this paper

$$
\text{Eqn. (5.1):} \quad \tilde{\nu}_c = a\left[\frac{1 - \lambda_N^{1+p}}{(1+p)(1-\lambda_N)}\right], \quad C_0 = a\left[\frac{\lambda_1^{1+p}}{1+p-n}\right], \tag{B 5a,b}
$$

$$
\text{Eqn. (5.2):} \quad \tilde{\nu}_c = a\left[\sum_{k=0}^p \binom{p}{k} \frac{(-1)^k(1-\lambda_N^{1+k})}{(1+k)(1-\lambda_N)}\right], \quad C_0 = a\left[\sum_{k=0}^p \binom{p}{k} \frac{(-1)^k \lambda_1^{1+k}}{1+k-n}\right]. \tag{B 6a,b}
$$

For each case, $a = (1+p)\tilde{\nu}_s$. The actual scheme used makes the following transformation:

$$
\omega_j = \omega_{N+1} - \rho_j \, \mathrm{e}^{\mathrm{i}(\vartheta_j + \theta_c)}, \tag{B 7}
$$

and recalling that $\omega_{N+1} = r_c \, \mathrm{e}^{\mathrm{i}\theta_c}$, the ϑ_j are then measured anticlockwise positive from the line connecting ω_{N+1} and the origin, and the ρ_j are the corresponding radii measured from ω_{N+1} to each ω_j. The angles ϑ_j are held constant and the values of λ_j are unknowns to be determined. Treating $\tilde{\nu}_s$ as unknown results in poor convergence as it quantifies the normal boundary condition on the sheet. Therefore, we instead take $\tilde{\nu}_o$ as unknown and specify $\tilde{\nu}_s$. By locating the wedge apex at $\omega_0 = 0 + i0$ and since $\lambda_0 = 0$, we then have a $2N + 4$ system of equations expressed by

$$
f(x) = 0, \quad x = (\rho_1, \rho_2, \ldots, \rho_N, \lambda_1, \lambda_2, \ldots, \lambda_N, r_c, \theta_c, J, \tilde{\nu}_o). \tag{B 8}
$$

For the cases with $\tilde{\nu}_o = 0$ and variable M in §4.2, the former was replaced with Θ as the unknown to be obtained. The system is iteratively solved with the fsolve function in Matlab until the Euclidean vector norm of $f(x)$ is less than $\epsilon = 10^{-10}$.

REFERENCES

BATCHELOR, G. K. 1967 *An Introduction to Fluid Dynamics*. Cambridge University Press.

BIRKHOFF, G. 1962 Helmholtz and Taylor instability. In *Proceedings of Symposia in Applied Mathematics*, vol. 13, pp. 55–76. American Mathematical Society.

BROWN, C. E. & MICHAEL, W. H. 1954 Effect of leading-edge separation on the lift of a delta wing. *J. Aeronaut. Sci.* **21** (10), 690–694.

DEVORIA, A. C. & MOHSENI, K. 2019 The vortex-entrainment sheet in an inviscid fluid: theory and separation at a sharp edge. *J. Fluid Mech.* **866**, 660–688.

ELLINGTON, C. P., VAN DEN BERG, C., WILLMOTT, A. P. & THOMAS, A. L. R. 1996 Leading-edge vortices in insect flight. *Nature* **384** (6610), 626–630.

JONES, M. A. 2003 The separated flow of an inviscid fluid around a moving flat plate. *J. Fluid Mech.* **496**, 405–441.

KRASNY, R. 1987 Computation of vortex sheet roll-up in the Trefftz plane. *J. Fluid Mech.* **184**, 123–155.

MOORE, D. W. 1979 The spontaneous appearance of a singularity in the shape of an evolving vortex sheet. *Proc. R. Soc. Lond.* A **365**, 105–119.

MUSKHELISHVILI, N. I. 1946 *Singular Integral Equations*, 1st edn. P. Noordhoof Ltd.

PULLIN, D. I. 1978 The large-scale structure of unsteady self-similar rolled-up vortex sheets. *J. Fluid Mech.* **88** (3), 401–430.

PULLIN, D. I. & PERRY, A. E. 1980 Some flow visualization experiments on the starting vortex. *J. Fluid Mech.* **97**, 239–255.

ROTT, N. 1956 Diffraction of a weak shock with vortex generation. *J. Fluid Mech.* **1**, 111–128.